NEAR-INFRARED BROAD-LINE PROFILES IN LOW-REDSHIFT QSOs

KEITH L. THOMPSON
McDonald Observatory and University of Texas at Austin[1]
Received 1991 November 18; accepted 1992 February 26

ABSTRACT

We present near-infrared and optical spectrophotometry of six low-redshift QSOs. The integrated Paα/Hα ratios cluster near the value 0.1, with one exception having a larger ratio consistent with other evidence of reddening. At least two of the Paα/Hα profile ratios decrease with observed velocity. We discuss some implications for the dynamics of the broad-line region and this ratio's usefulness as a reddening indicator. We also present a spectrum of the He I $\lambda 10830$, Paγ blend of 1226+023. The He I/Hα profile ratio shows marginal evidence for decreasing with observed velocity, which is consistent with the interpretation for the Paα/Hα profile ratios.

Subject headings: dust, extinction — infrared: galaxies — line: profiles — quasars: general

1. INTRODUCTION

During the last 10 years or so infrared spectroscopy of AGN has become an important tool, particularly with respect to the properties of the broad-line region. Even the early single channel continuously variable filter spectra (Grasdalen 1976; Puetter et al. 1978; Soifer et al. 1981; Puetter et al. 1981; Lacy et al. 1982; Rudy & Willner 1983; Le Van et al. 1984; McAlary et al. 1986; Yates & Garden 1989) have not yet been completely supplanted by more accurate measurements. More advanced instruments have, however, been used to good effect to study low-redshift broad-line objects, with higher resolution and lower noise (e.g., Sellgren et al. 1983, Ward et al. 1987, and Evans & Natta 1989). Infrared spectroscopy of rest frame optical lines of higher redshift objects, a more difficult prospect, has become much more successful with higher sensitivity (cf. Soifer et al. 1979, 1981; Puetter, Smith, & Willner 1979; Kühr et al. 1984; Espey et al. 1989). Recently, the study of highly reddened broad-line objects, for which there is little or no evidence for broad lines in the optical, has motivated the observation of several infrared lines, leading to discovery of broad Paα, Paβ, etc. in objects with little or no broad Hα (Blanco, Ward, & Wright 1990; Goodrich 1990; Rix et al. 1990; Hines 1991).

A particularly important aspect of the infrared line measurements for low-redshift AGN, besides the long-wavelength baselines useful for reddening study, is the increase in the number of line ratios available for emission region diagnostics. Two of the most sought lines are Paα and He I $\lambda 10830$, primarily because both are strong lines accessible with the instruments available, and are sensitive to several useful quantities. The He I $\lambda 10830$ line represents the lowest transition of the triplet states of He^o, and is sensitive to line trapping; the ratio to He I $\lambda 5876$ should be a strong function of incident flux, especially at large values. The Paα/Hα ratio is sensitive to optical depth and density (Kwan 1984).

The use of the Paα/Hα ratio to estimate reddening to the broad-line regions of AGN depends on the range of intrinsic values for the ratio. A number of researchers have noted some discrepant points (e.g., Puetter et al. 1981; Soifer et al. 1981; Lacy et al. 1982; McAlary et al. 1986), where the ratio is signifi-

cantly less than the more typical value 0.1, a decrease being inaccessible by way of reddening. Although numerous photoionization models predict low values of Paα/Hα, we may wonder why so few objects have such ratios. Currently available infrared spectrometers can now easily measure these line fluxes to the photometric accuracy needed to confirm these deviations. It follows that we now must pay attention to finer differences in observed Paα/Hα ratios, to facilitate use of the ratio both as a reddening indicator and as a broad-line cloud diagnostic.

Although the broad-line profiles of a single QSO appear remarkably similar to each other, it has long been recognized that they can have significant differences. Perhaps most obvious are the differences between Hα and He I $\lambda 5876$, and to a lesser extent Hβ (e.g., Shuder 1982, 1984; Crenshaw 1986). The implication is that the observed velocity is closely correlated with the broad-line cloud characteristics or conditions, giving us insight into the dynamics and structure of the broad-line region. Historically, the problem with pursuing this investigation has been the dearth of unblended lines with which one can make these detailed comparisons, along with the high noise and low resolution of the UV and infrared spectra generally available which could otherwise increase the sample of such lines. Observations using the *HST* and the modern generation of near infrared spectrometers can help address these issues. Although the infrared spectrometer used in the work presented here is now outperformed by more modern instruments, significant information about the broad-line profiles of QSOs can be extracted.

Section 2 details the Paα, He I $\lambda 10830$/Paγ blend, and optical spectrum observations and reductions for the sample of six QSOs. Section 3 describes the comparison of the infrared lines to Hα, both with respect to the integrated fluxes and the profile ratios. The discussion in § 4 addresses the use of Paα/Hα as a reddening indicator and investigates the profile differences in terms of cloud conditions and dynamics, followed by a summary in § 5.

2. OBSERVATIONS AND REDUCTION

2.1. Observations

The QSO sample includes the same six objects analyzed in Thompson (1991, hereafter T91). Table 1 lists the QSOs, along with magnitudes, redshifts, and Hα FWHM.

[1] Postal address: California Institute of Technology, Astronomy, Mail-code 105-24, Pasadena, CA 91125.

TABLE 1

OBJECT SAMPLE

Object (1)	Other Designation (2)	z (3)	$m_V{}^a$ (4)	$M_V{}^a$ (5)	FWHM of Hα (km s^{-1})[b] (6)
0804+761	PG	0.101	15.5	−23.7	2840
1211+143	PG	0.081	14.63	−23.9	1630
1226+023	PG, 3C273	0.159	12.8	−27.0	3170
13349+2438	*IRAS*	0.109	15.	−23.9	2220
1803+676	KAZ 102	0.136	15.78	−23.7	3190
21219−1757	*IRAS*	0.112	15.67	−23.4	2310

[a] Values taken from Véron-Cetty & Véron 1989, except for 21219−1757 where m_V was measured from the spectra in this work, and M_V was approximated using the same formula as used by Véron-Cetty and Véron.

[b] Values from this work, uncorrected for resolution effects.

The optical spectra were all obtained with the es-2 Cassegrain spectrograph on the 2.1 m Struve reflector at McDonald Observatory during three observing runs in 1987 and 1988. The (2 pixel) resolution was about 14 Å, corresponding to about 600 km s^{-1} at Hα. The east-west slit corresponded to 5″, and the seeing was between ∼1″ and 3″. See T91 for a description of the observations and some aspects of the reduction process not detailed below. Table 2 lists a log of the optical observations (cols. [3] and [4]). The spectra are displayed in Figures 1a–1f, along with the adopted continua as described below.

The infrared spectra were obtained with the infrared grating spectrometer (IRGS) at the f/18 Cassegrain focus of the 2.7 m reflector at McDonald Observatory (see Lester, Harvey, & Carr 1988 for a description). The fixed aperture corresponds to a 3″.8 square, which projects onto a single pixel of the detector. Most of the Paα spectra were taken with the low-resolution

grating, which gives a dispersion of about 0.0107 μm pixel^{-1}. For most of the objects, the grating was shifted by half a channel and a second spectrum was taken, allowing construction of a nominally Nyquist-sampled spectrum. This resulted in resolutions of about 220, or roughly 1400 km s^{-1}, for the low-resolution spectra. The Paα spectra are shown in Figures 2a–2f. Observations of 1226+023 were also taken with the high-resolution grating in the J-band over several epochs, shown combined in Figure 2g. The J-band observations were not Nyquist-sampled, and the dispersion was about 0.0024 μm pixel^{-1} (∼575 km s^{-1} pixel^{-1}). Table 2 includes a log of the infrared spectra in columns (6), (7), and (8).

2.2. Reduction

The optical images were reduced to one-dimensional spectra with an adaptation of the optimal extraction algorithm described by Horne (1986). The cross-dispersion profiles were

TABLE 2

OBSERVATION LOG

OBJECT (1)	$E(B-V)$ (2)	OPTICAL OBSERVATIONS			INFRARED OBSERVATIONS			
		Dates (3)	Exposures[a] (4)	Photometry[b] (5)	Dates (6)	Integration time[c] (7)	Comments[d] (8)	Photometry[b] (9)
0804+761	0.06	1988 Apr 09	1800	10%[e]	1988 Mar 26	2460	Paα: LRG, λ1 setting	10%
					1988 Mar 27	1800	Paα: LRG, λ2 setting	
1211+143	0.0	1988 Apr 11	2 × 1800	15	1988 Mar 24	1380, 1920	Paα: LRG, λ1 and 2	20
					1988 Mar 27	1080	Paα: LRG, λ2	
1226+023	0.02	1988 Apr 09	2 × 1200	5	1987 Apr 08	600, 600	Paα: LRG λ1 and 2;	10
		1988 Apr 11	3 × 1200		1987 Apr 08	960	He I, Paγ: HRG	
					1987 Apr 09	1200	He I, Paγ: HRG	
					1988 Feb 27	2820	He I, Paγ: HRG	
					1988 Mar 25	2340	He I, Paγ: HRG	
					1988 Mar 26	840, 960	Paα: LRG, λ3 and 4	
13349+2438	0.007	1987 Jul 30	2 × 1200	5	1987 Apr 09	720, 660	Paα: LRG, λ1 and 2	10
		1988 Apr 09	2 × 1800					
		1988 Apr 11	3 × 1800					
		1988 Jun 18	2 × 1800					
		1988 Jun 20	1800					
1803+676	0.05	1988 Jun 18	3 × 1800	15	1988 Jul 23	2520	Paα: LRG	10
		1988 Jun 19	2 × 1800					
		1988 Jun 20	2 × 1800					
21219−1757	0.04	1988 Jun 19	1200	15	1988 Jul 24	1320	Paα: LRG	15
		1988 Jul 20	1800		1988 Jul 25	300	Paα: LRG	
					1988 Sep 20	1380	Paα: LRG	

[a] Number of exposures and integration times (s).

[b] Estimated photometric reliability for the final co-added spectrum.

[c] On-source integration time (s); does not include sky integrations.

[d] LRG = low-resolution grating, MRG = medium, HRG = high; λ1 and λ2 refer to wavelength settings shifted by half a pixel, and λ3 and 4 for 1226+023 refer to a different pair (see text).

[e] Because of the nature of the observation, this error estimate is based on very little information.
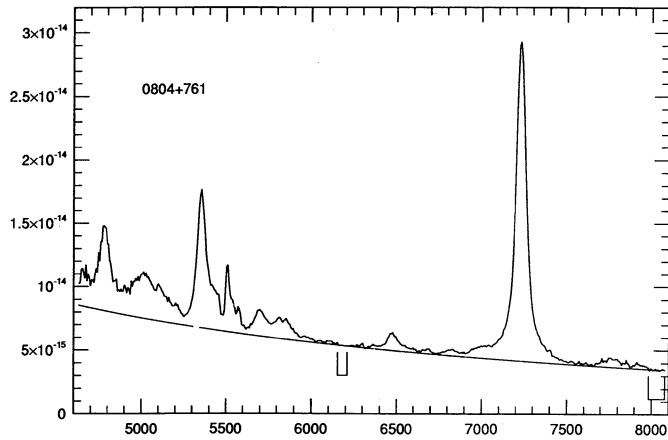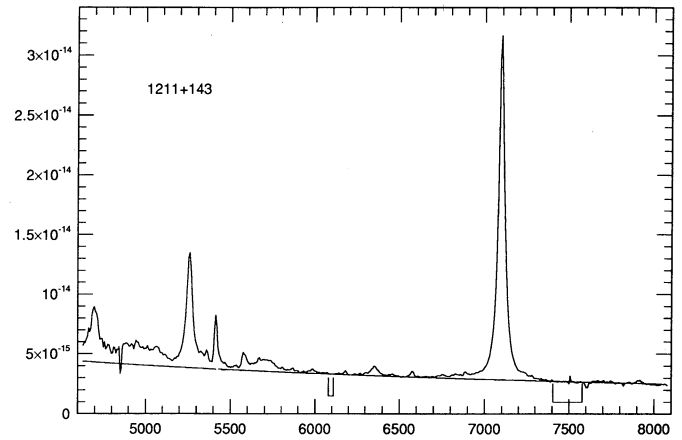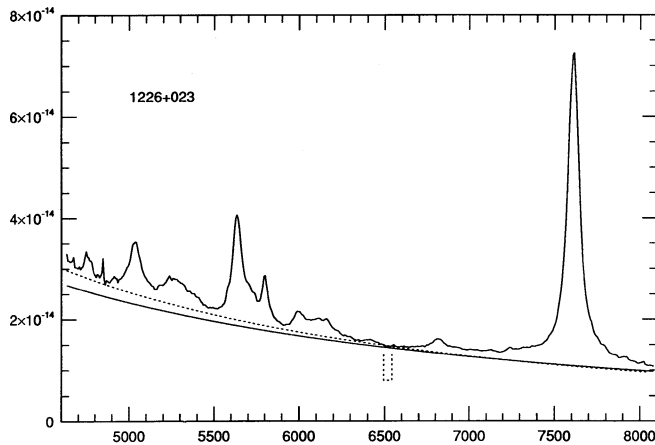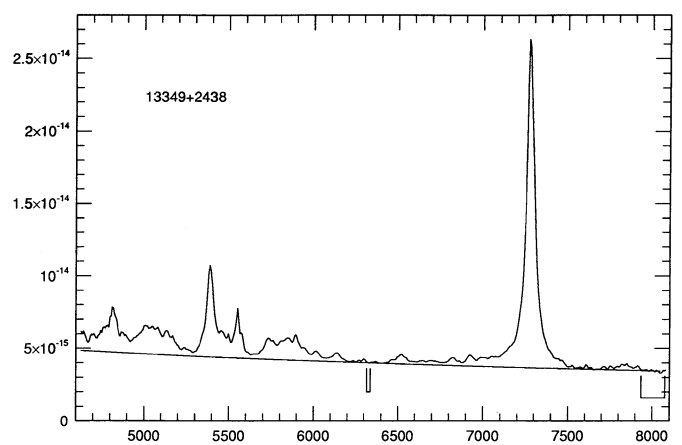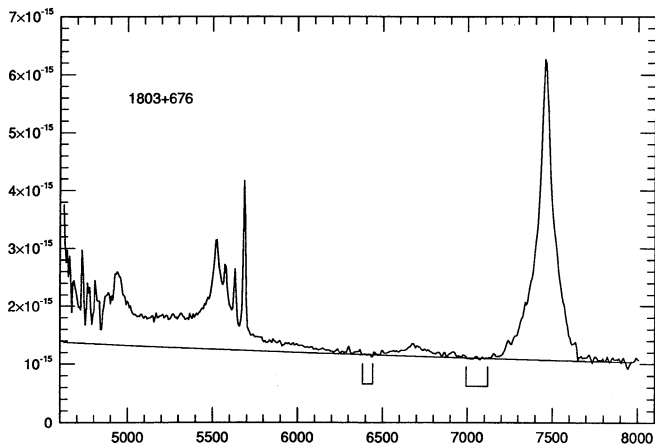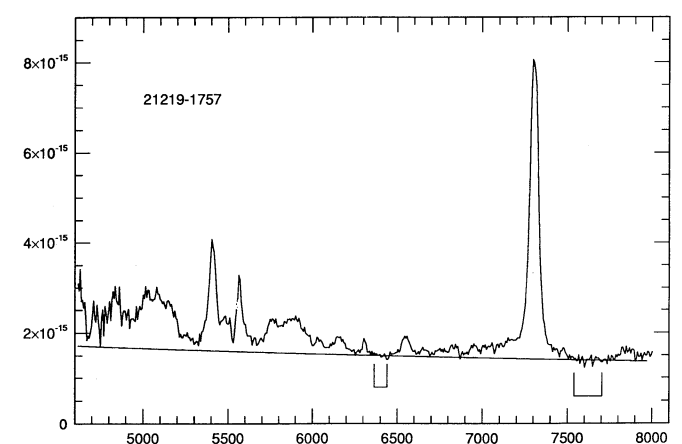
FIG. 1.—(a–f) Optical spectra of the six program QSOs. The plots display F_λ vs. observed wavelength in ergs s^{-1} cm^{-2} Å^{-1} and Å, respectively. The adopted (power law) continua are drawn beneath the spectra, with the intervals marked that were used to fit the power-law functions. For 1226−023, the dotted line represents the first estimate (see text).

determined by a running median filter rather than a polynomial, because the CCD had a charge transfer problem that made the profile depend somewhat on the intensity. The width of the median filter was chosen to be the largest such that the optimally extracted spectrum and the standard extraction were the same except for differences expected from noise, hot pixels,

or "cosmic ray" events. The resulting noise in the optimally extracted spectra was about a factor of 2 smaller than for the corresponding standard extractions.

The infrared spectra were observed with many exposures, using a sequence of "quads," each consisting of four one-minute integrations (on-source, off, off, on). A raw spectrum for
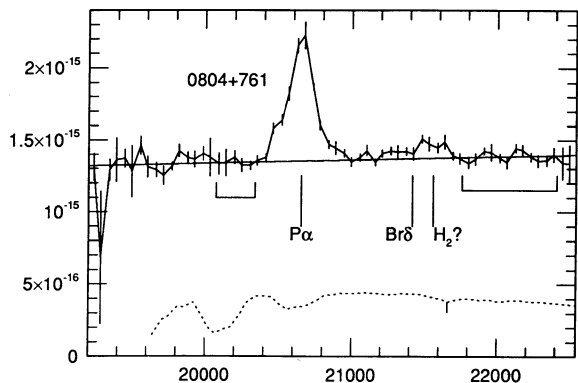
FIG. 2a
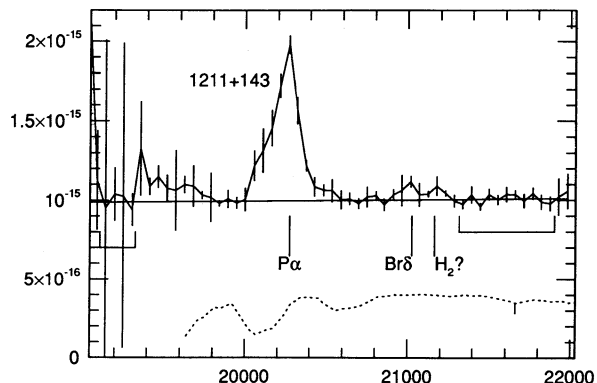
FIG. 2b
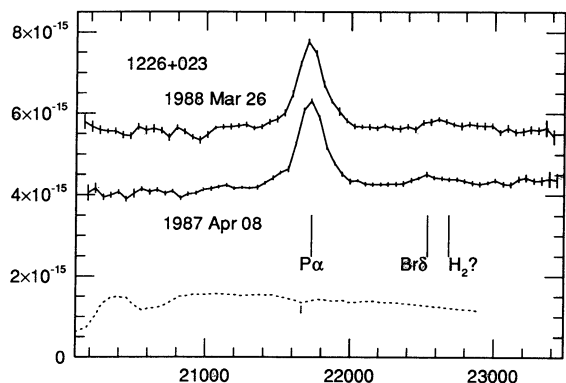
FIG. 2c
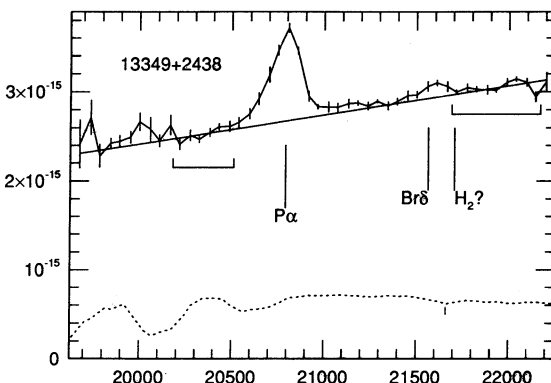
FIG. 2d
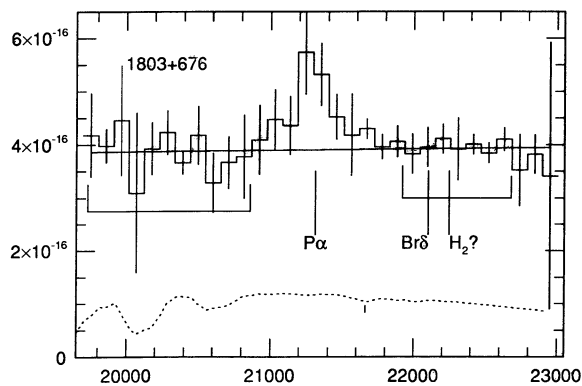
FIG. 2e
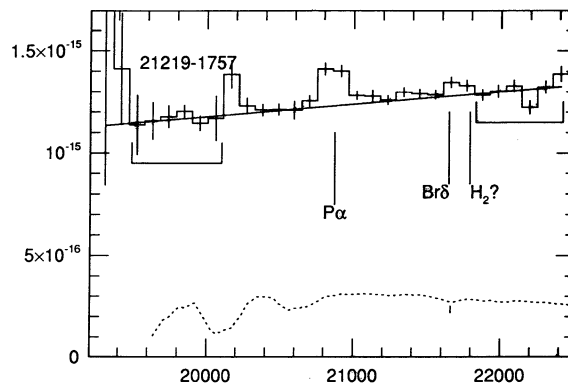
FIG. 2f
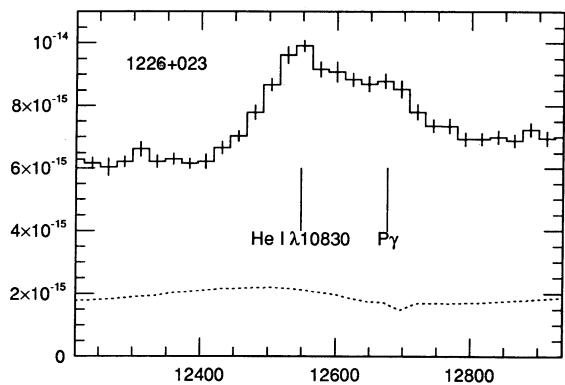
FIG. 2g
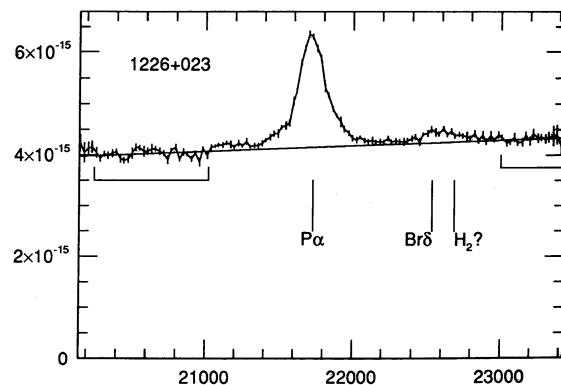
FIG. 2h

a sequence of quads was the sum of the object-sky differences. Generally, a sequence of quads was taken for an hour or less, with standard and sky division star observations before and after. Each sequence was reduced, calibrated, and corrected for atmospheric absorption features independently of other sequences, so that the range of time and air mass was small. If multiple sequences were taken of a QSO with the same grating setting, they were co-added with weights set according to the noise.

For the optical observations, broad-band atmospheric extinction was derived for each night using the multiple observations of bright stars, most having spectral types close to A0. The magnitudes as a function of wavelength were taken from Cochran (1981), interpolated to narrow bands following Oke (1964) with minor changes to avoid strong atmospheric absorption features. For the few nights where two photometric standards could independently be used to generate calibration functions, the functions differed by less than 4% at any point, and generally by ~1%. Such consistency may be fortuitous given that the expected uncertainty in Cochran's flux distributions is about this large. The infrared spectra were photometrically calibrated with bright star broad-band fluxes, and absolute photometric calibration listed in the IRTF Photometry Manual (Tokunaga 1986), assuming blackbody spectra appropriate for the spectral type to set the slope. The standard stars were observed close to the objects in air mass and time, and no additional broad-band extinction correction was made to either the standards or the QSOs, assuming the corrections would cancel within the errors inherent in the infrared observations.

Not all of the observations were taken in photometric conditions. The photometric spectra obtained for a QSO were used to rescale the nonphotometric spectra before co-addition. The photometric reliability of each final spectrum, listed in Table 2 (cols. [5] and [9]), was estimated from the consistency of multiple observations of the QSOs and the stars used for atmospheric extinction and photometric calibration.

Early-type stars were used to generate sky division templates which were used to remove the narrow atmospheric absorption features. The most important features were the A-, B-, and a-bands in the optical and the CO_2 features at ~20100 and 20600 Å in the infrared. Small shifts in wavelength between the standards and the QSOs, caused by imprecise guiding, sometimes caused "P-Cygni" profiles in the divided spectrum. These shifts were largely corrected in the optical division stars using interpolation, but the infrared spectra could not be shifted because raw IRGS spectra are not properly sampled, and furthermore with no more than two deep atmospheric features there was not enough redundancy to reliably determine the relative shifts. A representative sky division star is plotted in dotted lines beneath the QSO spectra in Figures 2a–2g, and in the K-band spectra the CO_2 features are clearly seen as broad dips at ~20100 and ~20600 Å.

The infrared spectra taken with half-pixel shifts relative to each other were combined after calibration. A linear function was multiplied by one in order to match it to the other, and the pixel values of the two were then interleaved into a single spectrum. A linear function was used rather than a single value because the IRGS generates spectra with small residual slopes caused by a slight misalignment between the detector array and the dispersion axis, so that the continuum slope of the final spectrum depends on the exact position of the object within the aperture (~10% across the spectrum in extreme cases). For 1226+023, low-resolution spectra were taken at two epochs, each with two mutually shifted grating settings. Because the resulting two-setting spectra from the two epochs were fortuitously separated in wavelength by about a quarter pixel, these were then combined with each other using the same process, but this time with only an additive constant used to match the two spectra. The resulting Paα spectrum for 1226+023, with four points per resolution element, is shown in Figure 2h.

The error bars were derived by comparing the different observations of each QSO. For the optical spectra, the number of observations for some objects was small, and a running average of the errors gives the best idea of the actual pixel-to-pixel noise. For 0804+761, only one exposure was obtained, and error bars could not be derived by this method, but when comparing Hα with Paα the relative noise is dominated by the infrared spectrum. For the infrared spectra, each on-source, off-source pair was compared with the others after renormalizing to the global mean integrated intensity, so the error bars representing pixel-to-pixel noise of the final spectrum could be estimated with reasonable accuracy.

The spectra were corrected for Galactic extinction in both the infrared and optical spectra using the values for $E(B-V)$ found in Table 2 (col. [2]), which were determined from the extinction maps of Burstein & Heiles (1982). The average interstellar extinction curve listed in Savage & Mathis (1979) was used.

Optical redshifts were determined using the center of the half-maximum points of Hα. The infrared spectra were reduced to the rest frame with the same redshifts, but there could be significant relative differences because both the optical and infrared apertures span at least one resolution element of the final spectra. In the case of the infrared spectra, one aperture width represents about 1500 km s^{-1}, so poor guiding could result in a relative shift of up to 750 km s^{-1}. Finite seeing, however, results in a significant decrease in signal with large guiding errors, and such data were not included in the final co-addition. However, we cannot discount errors in wavelength calibration of up to ~0.2 pixels, or about 300 km s^{-1}. We will discuss these possible shifts further below, both with respect to shifts between the QSO and its atmospheric division star and shifts between the optical and infrared spectra.

In the following figures, the spectra are shifted to the rest

---

FIG. 2.—(a–f) Paα spectra of the six program QSOs. The axes are drawn with the same units as Fig. 1a–1f. For Figs. 2a–2d, the spectra were Nyquist sampled by shifting the grating and taking a second observation, so that 1 pixel is two data values wide and represents the approximate resolution of the spectra. The adopted (linear) continua are displayed as for Figs. 1a–1f. The expected positions of Paα, Brδ, and the H₂ 1–0 S(3) lines are marked. Beneath each spectrum a representative sky division star is plotted with dotted lines; the 2.01 and 2.06 μm CO₂ sky absorption features are prominent, and the stellar Brγ line is marked. Note that at this resolution, the CO₂ feature causes a drop of about a factor of 2 at 20,000 Å over an interval of about one pixel. (g) He I λ10830, Paγ blend of 1226+023. The axes and sky division star are as displayed in Figs 2a–2f. No continuum was chosen for this spectrum (see text). The spectrum represents the sum of spectra from four nights taken with the same grating setting. (h) Combined 2 epoch spectrum of Paα for 1226+023 with the adopted continuum. Note that there are four data values for each pixel, so the spectrum is oversampled by a factor of ~2.

frame without changing the amplitudes. All wavelengths are in (vacuum) angstroms, flux densities in ergs s^{-1} cm^{-2} Å^{-1}, and velocities are represented by $c(\Delta\lambda/\lambda)$ in km s^{-1}.

2.3. *Continua and Line Profiles*

The estimation of optical continua was as described in T91. The continua were power laws, fit through the pixels indicated by the "u-shaped" marks in Figures 1a–1f. The positions were chosen such that a power law would pass through the "lowest" points of the spectra. For 1226+023, a slightly different continuum was adopted as a result of analysis of Hβ and the Fe II blends (see Thompson 1992). The first choice, shown by a dotted line in Figure 1c, is nearly the same as the final adopted continuum (*solid line*) in the region of Hα, and the difference is insignificant with respect to the Hα-Paα comparison.

The infrared continua were established in a similar manner, except that they were represented by linear functions. The lowest sections of each spectrum were chosen to represent the continuum, and these avoided the region presumably occupied by Brδ and possibly H_2 1–0 S(2), as shown in Figures 2a–2f and 2h, except for 1803+676 where the feature was not detected. The case B ratio for Brδ/Paα is roughly 0.1, and the amplitudes of the bumps in the spectra are consistent with a line of about that intensity.

The Hα profiles were prepared for comparison with the infrared lines in the same manner as described in T91. The function used to degrade the resolution of the Hα profiles was a boxcar corresponding to the width of the infrared spectrometer pixels. The intrinsic resolution of the Hα profiles approximated the seeing/guiding plus instrumental point spread function of the infrared spectra, and therefore the boxcar alone was deemed sufficient. The most likely error in this assumption is that the Hα profiles are not degraded in resolution enough, which should slightly increase the differences between the Paα and Hα profiles found below if corrected more exactly.

2.4. *Variability*

The spectrum of 1803+676 displayed in Figure 1e was taken at a later epoch than the optical spectrum taken by the author that was used by Evans & Natta (1989). The second epoch was used in the present work because it was taken within 40 days of the infrared spectrum, even though the photometric accuracy of the second epoch is less certain. When dividing the first epoch spectrum (1987 July) by the second epoch spectrum (1988 June), Hα and Hβ appear in "emission" by ~20% and ~12%, respectively, implying a decrease in the equivalent width of the lines. Unfortunately, the estimated relative photo-

metric uncertainties of the two spectra (~15%) prevent reliable determination of whether the continuum level increased or the line fluxes decreased slightly during the intervening period; the average spectrum ratio is about 0.9 which is consistent with either interpretation.

The second epoch Paα spectrum of 1226+023 was taken during a period of UV, optical, and infrared flux variation in early 1988 (Courvoisier et al. 1988). The largest flare during that period was detected on March 9 of that year, about 17 days before the second Paα spectrum. Indeed, the K-band continuum flux is about 40% larger in the second spectrum than the first (Fig. 2c). From the excellent match between the line fluxes and profiles of the two Paα observations, we can conclude that the flares had a minimum impact on the broad-line clouds in aggregate. This may be because the broad-line region is much larger than 17 light days, or because the broad-line region is much larger than the duration of the flare, which determines the fraction of the broad-line region that can be affected by the flare at any moment of observation.

3. LINE COMPARISONS

3.1. *Average Flux Ratios*

A first-order method for comparing integrated fluxes of various lines is to fit the amplitude of the Hα profile at the position of the lines, as was done in T91 for He I λ5876 and Na I. Some information on the relative profile shapes can be determined from the residuals of the fits. However, it is most useful for the determination of an average ratio, because the fit will be weighted to the higher points of the line profiles. To the extent that the profiles have the same shape, the fit will reduce the noise in the ratio determination compared with the ratio of the simple line integrations, and for profiles that do not have the same shape the resulting value represents a weighted average of the profile ratio.

Table 3 displays the line ratios generated by fitting the Hα profile to the Paα profile, as well as the ratios derived for He I λ10830/Hα and Paγ/Hα for 1226+023. The quoted errors include both noise and photometric uncertainties. Sections of the spectra were excluded from the fits where improperly corrected atmospheric absorption features apparently interfered with the line profile (see below). Table 3 also lists Hβ/Hα ratios derived in a manner similar to Paα/Hα, with the addition of a simultaneous fit of the strengths of the numerous Fe II blends found around Hβ (Thompson 1992).

The infrared line fluxes of several of these objects have been reported previously in the literature. Table 4 shows some of these values for 1211+143, 1226+023, and 1803+676, adjust-

TABLE 3
FITS OF LINES

Object (1)	Hβ/Hα[a] (2)	Paα/Hα (3)	Paγ/Hα (4)	He I λ10830/Hα (5)
0804+761	0.291 ± 0.006	0.099 ± 0.004	...	...
1211+143	0.277 ± 0.005	0.119 ± 0.013	...	...
1226+023	0.240 ± 0.002	0.097 ± 0.002	0.043 ± 0.004	0.095 ± 0.004
13349+2438	0.205 ± 0.002	0.139 ± 0.005	...	...
1803+676	0.227 ± 0.004	0.105 ± 0.010	...	...
21219−1757	0.245 ± 0.009	0.102 ± 0.007	...	...

[a] The Hβ/Hα ratio was determined in a similar manner to He I and Na I as described in T91 and He I and Paγ for 1226+023 described in this work, but with Fe II blends included in the fits (Thompson 1992).

TABLE 4
COMPARISON OF INFRARED LINE INTEGRATED FLUXES

Object (1)	Hα flux[a,b] (2)	Paα flux[b] (3)	He I λ10830[b] (4)	Paγ[b] (5)
1211+143	16.6	2.0 (0.4)[a]	...	...
		2.2 (0.2)[c]		
		2.7 (0.5)[d]		
1226+023	80.7	7.8 (0.8)[a]	7.7 (0.8)[a]	3.5 (0.5)[a]
		6.7 (0.8)[e]	5.8 (1.6)[f]	
		5.0 (32%)[g]	10.0[h]	3.5[h]
		5.4[i]		
		4.7[h]		
		6.1 (0.6)[d]		
1803+676	6.24	6.6 (0.9)[a]	...	...
		6.9 (0.7)[j]		

[a] This work.
[b] Units 10^{-13} ergs s^{-1} cm^{-2}, corrected for Galactic reddening with values of $E(B-V)$ from Table 2, and errors including photometric uncertainty.
[c] Soifer et al. 1981.
[d] Yates & Garden 1989.
[e] Grasdalen 1976.
[f] LeVan et al. 1984; the value represents the sum of He I λ10830 + Paγ.
[g] Puetter et al. 1981; note that the same data first appeared in Puetter et al. 1978, but was apparently rereduced for the 1981 paper.
[h] Ward et al. 1987.
[i] Sellgren et al. 1983.
[j] Evans & Natta 1989.

ed to the observed frame and corrected for the Galactic reddening values specified in Table 2 in order to facilitate comparison.

The values from different instruments, authors, and epochs agree reasonably well in most cases, but there are notable exceptions for 1226+023. First, this work's Paα flux for this object is greater than any of the other values. It is consistent with both of the other values that have published uncertainties, but not the two without uncertainties if we can assume errors less than 20%. One possible explanation, beyond intrinsic variation in the strength of the lines, is the different determination of the continuum. In the present work the continuum was made as low as possible consistent with a large wavelength range to either side. The spectrum by Sellgren et al. (1983) (and possibly the spectrum by Ward et al. 1987) did not cover as large a wavelength range and the authors may have chosen a higher continuum because of the extended Paα wings. Second, the He I λ10830 line flux of the present work differs from the Ward et al. value, and might again be caused by the difference in chosen continuum. Although the Ward et al. spectrum covered a somewhat larger wavelength interval, they did not specify their method of continuum determination or their method of measuring the lines. The He I + Paγ flux also disagrees strongly with the LeVan et al. (1984) value, but this might be explained by a single bad datum; their spectrum contains only two points with significant amplitude above the continuum level, and the apparent position of the line is not coincident with the expected position.

Figure 3 displays a plot of the ratios of Paα/Hα versus Hα/Hβ as listed in Table 3. Also shown for 0804+761, 1226+023, and 13349+2438 are the central value ratios, displayed as open circles connected to their respective average values with small line segments. The large circle represents the case B ratios, and the line extends along the reddening line out to $E(B-V) = 0.5$.

The points in Figure 3 provide no surprises. We can compare this diagram with similar figures in Puetter et al.

(1981), Soifer et al. (1981), Lacy et al. (1982, Seyferts only), McAlary et al. (1986), Evans & Natta (1989, includes most of the earlier works' values as well as their two new points), and Yates & Garden (1989). Given the somewhat smaller uncertainties of the present sample ratios, we expect somewhat smaller dispersion in the values, and indeed we find the new set of values well centered in the scatter of QSOs shown in Evans & Natta's figure.

3.2. Paα/Hα Profile Ratios

Figures 4a–4f show the Paα/Hα profile ratios, with the Paα and degraded Hα profiles plotted below for comparison. The values for Hα were interpolated with a cubic spline to match the pixel positions in the Paα profiles. In the following discussion we will use $+v_{25}$ and $-v_{25}$ to represent the red and blue half-widths at 25% maximum of Hα, with corresponding definitions for $\pm v_{10}$, etc. Beneath each profile ratio in Figures 4a–4f are two bars, representing the intervals between $-v_{10}$ and $+v_{10}$ and between $-v_{25}$ and $+v_{25}$. The Hα and Paα profiles were plotted with relative expansion factors corresponding to the integrated ratios of Table 3, and beneath the profiles are heavy lines representing the velocity domain used in the fitting routine that resulted in those ratios.

Note that the error bars come from the quadrature sum of the fractional errors of the Paα and Hα pixel values, and do not include photometric uncertainty. Therefore, the error bars in Figures 4a–4f and the errors quoted in the following section represent relative and not absolute uncertainties in the ratio.
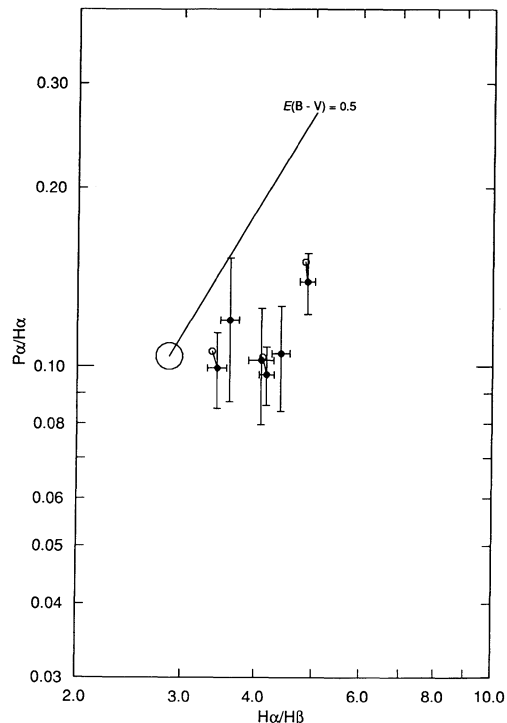
FIG. 3.—Integrated Paα/Hα ratio vs. the Hα/Hβ ratio, with values from Table 3. The large circle represents case B-values, and the line extends out along the reddening line to $E(B-V) = 0.5$. The error bars include relative photometric uncertainties as well as the uncertainties involved in the profile fits. Three objects (0804+761, 1226+023, and 13349+2438) also have small circles plotted which represent their line center ratios, which are connected to their respective integrated ratios with small line segments.
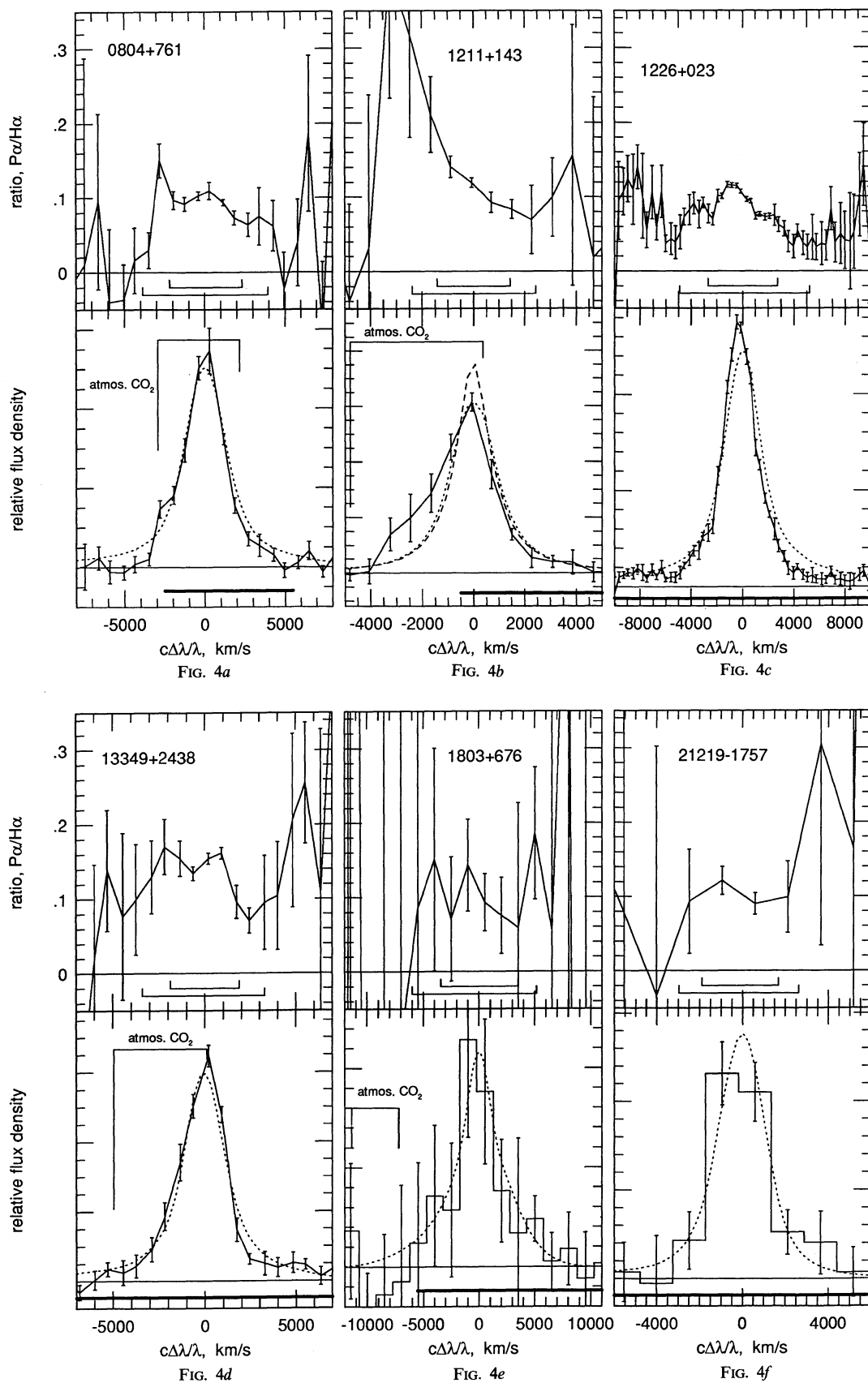
FIG. 4.—(a–f) Paα and Hα profiles and profile ratios. The two bars below each profile ratio represent the interval from $-v_{10}$ to $+v_{10}$ and $-v_{25}$ to $+v_{25}$. The convolved Hα profiles in the bottom panels are plotted with dotted lines. In addition, the original unconvolved Hα profile of $1211+143$ is also plotted with a dashed line for comparison; $1211+143$ has the narrowest Hα profile of the sample. Atmospheric absorption features are also marked to facilitate comparison with Figs. 2a–2f.

It is important also to note that the line profiles were not corrected for either narrow hydrogen components or the forbidden lines [N II] $\lambda6548$, $\lambda6583$. No inflection points are seen in the optical broad lines that might indicate narrow components to the hydrogen lines, and any small components that may exist must perforce be considered as part of the broad lines. The [N II] lines cannot have significant intensity because there are no dips at their corresponding positions in the Hβ/Hα profile ratios (not shown).

It is appropriate to discuss each object in some detail:

0804+761.—The blue wing of Paα in 0804+761 seems to have interference from the blue edge of the 20600 Å CO_2 atmospheric absorption feature, apparently caused by a slight wavelength shift between the object and the sky division star. Since the red side of this CO_2 feature is more gradual, its influence should be much smaller. The red wing shows a decrease in the Paα/Hα ratio with velocity. If the slight wavelength shift is a correct explanation of the blue wing feature, the shift involved is of order 10% of a pixel, which corresponds to about 150 km s^{-1}. Although it is in the right direction to "correct" the ratio decrease on the red wing, a shift of about 1000 km s^{-1} is required to make a significant difference, and even then would cause a large asymmetry in the ratio at small velocities. On the other hand, the continuum could be overestimated, with a quasi-continuum built up on both sides by blends of unidentified lines, which fortuitously do not exist right at Paα itself. In order that the profiles be made consistent, this hypothetical morass of blended lines must generate a quasi-continuum of larger amplitude than the height of the one feature actually seen to the red of Paα (consisting of Brδ and perhaps other lines). We will not consider this possibility further, and assume that the chosen continua of the K-band spectra represent the actual continuum levels with an accuracy better than the pixel to pixel noise of the spectra.

The previous arguments suggest we can use the Paα/Hα profile ratio of 0804+761 as originally analyzed, with the exception of part of the blue wing. Measurement of the average of the profile ratio of the main core, in the interval $-v_{25}$ to $+v_{25}$, yields Paα/Hα = 0.095 ± 0.04, and the segment between $+_{25}$ and $+v_{10}$ has the ratio 0.070 ± 0.021 (involving 6 and 2 pixels, respectively). Note that the blue wing range includes a point with particularly high noise; the actual trend in the ratio is best verified by using all the pixels at once. All but one of the pixels out to ±6000 km s^{-1} have values smaller than the central two pixels, most by more than 1 σ, with the single exception probably affected by atmospheric absorption.

1211+143.—The K-band spectrum of 1211+143 is problematic. The red half of the profile, out to $+v_{10}$ or so, is found between the two CO_2 atmospheric absorption features. The blue side is observed through the 20100 Å feature. The pixel at about -4000 km s^{-1}, which is at about 20,000 Å in the observed frame, is on the steeper side of the absorption feature, and if there were any small wavelength shifts, this pixel would be affected most. The apparent excess flux on the blue side of Paα might be caused by a poor atmospheric division, but this explanation is not entirely satisfactory because the air masses of the object and the sky division stars were reasonably well matched. On the other side, the red half of the profile shows a decrease in the Paα/Hα ratio with velocity. Although the apparent decrease on the red side can be significantly reduced by a shift in the wavelength scale by ~ 300 km s^{-1} ($\frac{1}{5}$ pixel), the agreement in wavelength between the object and the sky division star indicated by the pixel at -4000 km s^{-1} suggests that

a wavelength shift is not responsible. The wavelength calibration and centering of bright stars in the aperture is more reliable than for faint sources which are observed for longer periods, and we can conclude that the absolute wavelength scale on the object is probably accurate to much better than $\frac{1}{5}$ pixel (which would cause a bump or dip of order 10% in the original spectrum at $\sim 20,000$ Å). Therefore, we can maintain that the profile ratio likely decreases with velocity on the red side. The three central pixels give an average Paα/Hα ratio of 0.118 ± 0.007 [$-v_{25}$, $+v_{25}$], and the two pixels in the red wing between $+v_{25}$ and $+v_{10}$ give a ratio of 0.077 ± 0.024, a marginal decrease. Further observations are necessary at higher resolution and tighter wavelength control to determine if the blue side "excess" is real and to confirm the red side ratio decrease.

1226+023.—With 1226+023, we have two separate epochs plotted in the same spectrum, and therefore have more data to test consistency. The redshift puts the Paα profile well away from the atmospheric CO_2 absorption features as well. We can see that the profile ratio of Paα/Hα definitely decreases with velocity on either side, having a central value of greater than 0.10 and a value perhaps as low as half the central ratio at the v_{10} velocities. The centers of the Paα and Hα profiles appear to be slightly displaced. A shift of 270 km s^{-1}, just under $\frac{1}{5}$ of a pixel, is enough to make the profile ratio nearly symmetric. That the two independent observations of Paα seem to have very similar positions suggests that any error is likely to be systematic and not simply the result of the object being poorly centered in the aperture. We shall assume that the asymmetry is real; it does not affect our conclusions. The central [$-v_{25}$, $+v_{25}$] section has the ratio 0.091 ± 0.002, and the two wings have the ratios 0.078 ± 0.007 and 0.046 ± 0.005 for the blue and red wings, respectively ([$-v_{10}$, $-v_{25}$] and [$+v_{25}$, $+v_{10}$]), corresponding to a 2 σ decrease from the line core for the blue wing and a 9 σ decrease for the red wing. If the center ratio is taken from the [$-v_{75}$, $+v_{75}$] interval (5 pixels; 0.106 ± 0.002), the blue and red wing decreases correspond to 4 σ and 12 σ, respectively.

One feature of the Paα spectrum of 1226+023 that deserves remark is the flattening of the spectrum between about $+5000$ and $+10,000$ km s^{-1}. Such a flattening is extemely unlikely to be caused by blended lines. Even another line at 15,000 or 20,000 km s^{-1} of similar amplitude to Paα would not produce such a flat interline spectrum, but would produce a sharper minimum. The best explanation is that the flux from Paα is nearly zero where the spectrum flattens, and the profile is converging toward the continuum. The conclusion must therefore be that the decrease in the Paα/Hα ratio with velocity is real.

13349+2438.—The Paα spectrum of 13349+2438 might have an effect from the CO_2 absorption features caused by small wavelength shifts. At about 20,000 Å where the effect should be largest, because the slope of the atmospheric absorption spectrum is greatest, we see in Figure 2d a small bump. Since the slope at 20,000 Å is roughly 2 or 3 times as steep as at 20,500, we expect an excess $\frac{1}{2}$ or $\frac{1}{3}$ as large as the roughly 10% apparent excess at 20,000 Å. Correction for this presumed systematic error would reduce the pixels at about -4000 km s^{-1} in Figure 4d by roughly 1 σ, thereby creating a difference greater than 1 σ between the Hα and Paα profiles in the blue wing. The red wing is unaffected by such shift errors, and shows an excess of Hα over Paα for several pixels. It is all marginal, however, and few Paα pixels have values significantly different than the scaled down Hα profile, but the suggestion is

that the Paα profile has weaker wings than the Hα profile. A direct measurement of the ratios using the unmodified profile gives 0.140 ± 0.007 at the center and 0.071 ± 0.017 in the red wing ([$-v_{25}$, $+v_{25}$] with 5 pixels, and [$+v_{25}$, $+v_{10}$] with 1 pixel, respectively).

1803 + 676.—The Paα spectrum of 1803 + 676 was not Nyquist sampled, but the line is broad enough that we can potentially get some profile information from it. However, the apparent agreement between Paα and Hα is not of high reliability given the noise of the former, although the profile ratio is consistent with being constant with velocity.

21219 − 1757.—The spectrum of 21219 − 1757 is also not Nyquist sampled, and although its width is too narrow to determine much from such a spectrum, the relative noise in the Paα spectrum is much lower than for the previous object. Although only 4 pixels are expected to have any substantial flux from the line, all four are indeed consistent with the profile of Hα.

It must be mentioned that an apparent decrease in the Paα/Hα ratio depends on the accuracy of the removal of the blends in the wings of Hα. These lines are primarily Fe II blends on the blue wing, and the strongest on the red wing is [S II]. Because the Fe II features on the red side of Hα tend to be much weaker than on the blue side (see, e.g., Wills, Netzer, & Wills 1985), and the narrow [S II] lines are easier to remove with confidence, that the ratio appears to decrease in both wings of the profiles of 0804 + 761 and 1226 + 023 increases our confidence in the result. Furthermore, it is the red wing of 1211 + 143 and of 13349 + 2438 that suggests a similar result.

The continuum determinations are also critical to the results, but with the use of large wavelength range we argue that the adopted continua for most of the objects are robust. The determination for 1226 + 023, without a continuum point to the red of Hα, is problematic and cannot be addressed with the current spectrum. However, the highest reasonable continuum, with the zero-intensity points at $\lambda_{obs} \sim 7200$ and 8000 Å, would only increase the $\pm v_{25}$ and $\pm v_{10}$ Paα/Hα ratio values by roughly 10% and 20%, respectively, not enough to remove the significance of the ratio decrease.

In summary, both wings of Paα of 0804 + 761 and 1226 + 023 are weaker than the Hα profiles' wings, although the blue wing of 0804 + 761 has interference from atmospheric absorption. The red wings of 1211 + 143 and 13349 + 2438 both show the same effect, with lower significance, but their blue wings may have atmospheric problems which make the apparent excess fluxes equivocal. The average ratios of those objects are close to 0.10, with the exception of 13349 + 2438. The profiles of 1803 + 676 and 21219 − 1757 do not have sufficient profile information, but do have average Paα/Hα ratios very nearly 0.10 also.

3.3. He I λ10830 and Paγ

Figure 5 displays the fit of Hα profile at the positions of He I λ10830 and Paγ for 1226 + 023. Because this spectrum does not cover a sufficient wavelength range to get an independent estimate of the position of the continuum, a linear continuum was fit simultaneously. Because the continuum was fit rather than independently determined, such that the residuals were minimized under the assumption of He I and Paγ profiles exactly like Hα, we lose precise information on the actual profile shapes of He I and Paγ. Although the integrated flux ratios should be accurately estimated, the resulting profiles must be heavily influenced by this assumption used to estimate the
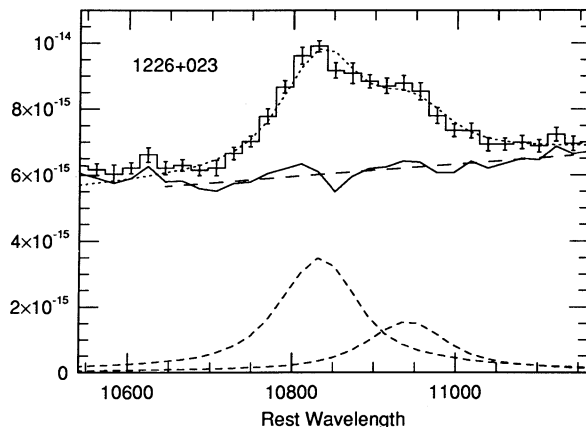
FIG. 5.—Fit of the Hα profile to He I λ10830 and Paγ for 1226 + 023. A linear continuum was fit at the same time, shown by the dashed line. At the bottom are the two Hα profiles scaled to the fitted amplitudes, and the dotted line represents the sum of the profiles and the fitted continuum. The residuals (spectrum minus the two scaled Hα profiles) are represented by the solid line passing through the continuum. Note that except for two pixel values, all the data values near the center of the He I and Paγ line positions are greater than the fitted spectrum, and many of the pixel values in the wings of the lines have negative values relative to the fitted spectrum.

continuum, and profile ratios thus derived should be viewed with caution; we do not even plot them here, especially because there is no simple way to separate He I from Paγ. In the appearance of the residuals, however, there is some suggestion that the wings of the He I profile are not as strong as Hα. A lower noise, higher resolution spectrum with larger wavelength coverage is necessary to remove the basic ambiguity of the continuum, particularly by identification and avoidance of weak features at the positions where the continuum is to be estimated. The spectrum in Ward et al. (1987) and another shown in Ward (1990), for example, have bumps at about 10560 Å (rest) that seem to match a bump in the spectrum presented here; although in Ward et al. (1987) and in our spectrum the feature has roughly a 2 σ amplitude, it must still bias any continuum estimation unless avoided.

4. DISCUSSION

4.1. Reddening

We can compare Figure 3 with a similar figure containing much of the early Paα data (Fig. 3 in Evans & Natta 1989). The objects in the present sample fall well within the confines of the group of QSOs, much as one would expect if a substantial part of the scatter of earlier measurements represents larger uncertainties than for the present sample. Most of the Paα/Hα ratios are close to 0.1; the exception is 13349 + 2438 with Paα/Hα = 0.14, which has other evidence for reddening (Wills et al. 1988). The appearance of Figure 3 suggests that the integrated Paα/Hα ratio might be more consistent than Hα/Hβ from object to object, and the tight distribution suggests that the sample (excluding 13349 + 2438) has small reddening values. The scatter of the other five ratios corresponds to a scatter in $E(B-V) \approx 0.04$ if reddening alone is responsible for the distribution of observed ratio values. Nevertheless, the individual drops in the Paα/Hα profile ratio with velocity for some objects demand that the ratio can vary within an individual broad line region.

We ask the question: is the integrated flux ratio of Paα/Hα a useful reddening indicator? Perhaps so, if the cores of the lines

are generated by clouds that are similar from object to object, even though some flux comes from regions which generate a significantly different Paα/Hα ratio. Such low Paα/Hα regions may not be represented in the same proportion from object to object, and therefore significantly modify the integrated ratios. We could use the central ratios, but these measurements are more sensitive to resolution and require good S/N and high resolution at the same time, and can be significantly affected by narrow components. Moreover, since we know the intrinsic ratio is not constant everywhere even within a single broad-line region, we can only trust some measurable quantity (central value, integrated flux ratio, etc.) as an empirical reddening indicator after detailed comparison with other reddening indicators.

4.2. Dynamics

The Paα/Hα profile ratios that decrease with observed velocity must be explained. Kwan & Krolik (1981) and Kwan (1984) show plots of the Paα/Hα ratio for several of their models for sequences with varying Lyman continuum optical depth. In general, larger optical depths have lower ratios, as well as larger densities for a given optical depth. There are not enough models plotted, however, to get an idea of how the ratio depends on ionization parameter, or alternately incident ionizing flux. We should also further organize the information in order to make a more coherent picture.

For the sake of analysis, let us initially postulate a kinematic system where the clouds are distributed in radius and have the highest velocities close to the central ionizing continuum source, such as a system dominated by gravitational dynamics. The wings of the lines, which must come from the small-radius clouds, must have ratios corresponding to high incident ionizing flux compared with the cores of the lines, which must come from a combination of small and large radius clouds.

We can postulate a system of clouds with any combination of the parameters hydrogen density n_H, ionization parameter U and column density N_H at any radius. However, we may reasonably assume that there is continuity to the run of the parameter values with radius. Following Rees, Netzer, & Ferland (1989), we shall make the assumption that the density is a function of radius, approximating a system where the clouds are confined by a pressure that varies with radius. Let us constrain the density as a function of radius by

$$n_H(r) \propto r^\gamma . \tag{1}$$

Note that the quantity $c n_H U$ is equal to the incident ionizing photon flux density, so $n_H U \propto r^{-2}$ for a point source and we can write

$$n_H(r) \propto (n_H U)^{-\gamma/2} , \tag{2}$$

which relates n_H to U for a given γ, and removes r from active participation in the relation.

By specifying a value for γ, the change in density n_H as a function of incident flux (or radius) is fixed. We can then look at sequences of models that are consistent with the density relation of equation (2), to see how the line ratios should vary with incident flux. For each value of γ, there are several density—ionization parameter model sequences that follow equation (2) but are mutually exclusive of each other, and these are represented by fiducial densities n_0 (defined as the density at which $n_H U = 10^{10}$ cm^{-3}).

A cloud system following equation (2) with $\gamma = -1$, for example, will have some value of this fiducial density n_0. When

dividing up the cloud models into different sequences, we find four (for $\gamma = -1$), each with a different characteristic n_0. Therefore by looking at plots, each containing models with a unique γ and n_0, we see the individual cloud models grouped together into physically self-consistent families representing clouds in the same system but with various incident fluxes.

We will investigate three values of γ: 0, -1, and -2. Constant density corresponds to $\gamma = 0$, where the variation of incident flux with radius depends entirely on U. The $\gamma = -2$ relation corresponds to constant U, where variation in incident flux depends on variation in density. The value of $\gamma = -1$ corresponds to both U and n_H varying in unison with radius.

Figures 6a–6c show the ratio of Paα/Hα, plotted against $n_H U$ for $\gamma = 0$, -1, and -2, respectively, for a grid of models run with the photoionization code Cloudy (Ferland 1990; see T91 for details on the parameter values used). The markers are ordered by size according to their values of hydrogen column density N_H, larger markers corresponding to larger values. Because equations (1) and (2) make no restriction on N_H, many values of N_H can have a single $n_H U$ value for a given γ and n_0.

The models plotted in Figures 6 are a subset of the grid described in T91, specifically those with predicted He II $\lambda4686$/Hα ratios less than 0.1. The largest amplitude of the blend in the objects at $\lambda4686$ corresponds to a line center ratio of 0.03, and since much of the flux at that point in the spectrum must be Fe II, 0.1 is certainly a safe upper limit to the line even allowing for uncertainties in the models. The parameter values eliminated represent the highest density ($n_H = 10^{11}$ cm^{-3}), high ionization parameter clouds ($U = 1$ and some 0.1), as well as some low-density clouds (10^8 cm^{-3}) that are optically thin.

We see that the Paα/Hα ratio tends to lower values for high incident fluxes, or at least stays approximately constant. Because we chose three quite different dependencies for the variation of n_H with radius, the dependence of the ratio with incident flux appears robust. Note that even free variation of the column density cannot produce a significant increase of the ratio with incident flux except at large $n_H U$ for $n_0 = 10^{12}$ cm^{-3} for the $\gamma = -2$ density law (representing one single cloud model).

Figures 7a–7c represent the He I $\lambda10830$/Hα ratios. We see a similar trend as with Figure 6: essentially all the model sequences show a decreasing or approximately constant ratio with increasing incident flux for all three density laws. A similar plot of the Paγ/Hα ratio (not shown) has the same property.

Although for most of the objects in our sample the evidence for a Paα/Hα (and He I/Hα) decrease with observed velocity is somewhat ambiguous even if suggestive, for at least 1226+023 and 0804+761 there is a clear inverse correlation between the Paα/Hα profile ratio and the observed velocity. From the photoionization models plotted above, we can explain this correlation by a correlation between the incident flux of the clouds and their representative velocity. This is consistent with gravitationally dominated cloud dynamics, and is inconsistent with radial outflow radiation-accelerated cloud systems, which should show an inverse correlation between velocity and incident flux. It is also consistent with the He I $\lambda5876$/Hα profile ratios observed in a number of low luminosity objects (Shuder 1982, 1984; Crenshaw 1986), which have also been explained by increased incident flux for the high-velocity clouds. It is interesting to note that 1226+023 and 0804+761 are two of the objects in T91 that appear also to have He I $\lambda5876$/Hα ratios which increase with velocity (the other is 1803+676).
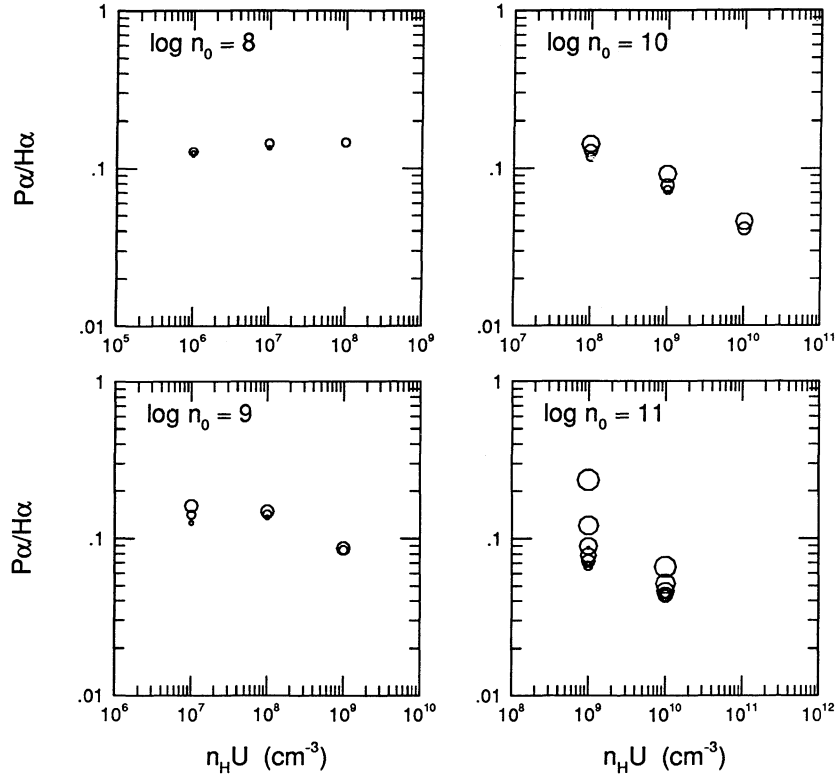
FIG. 6a
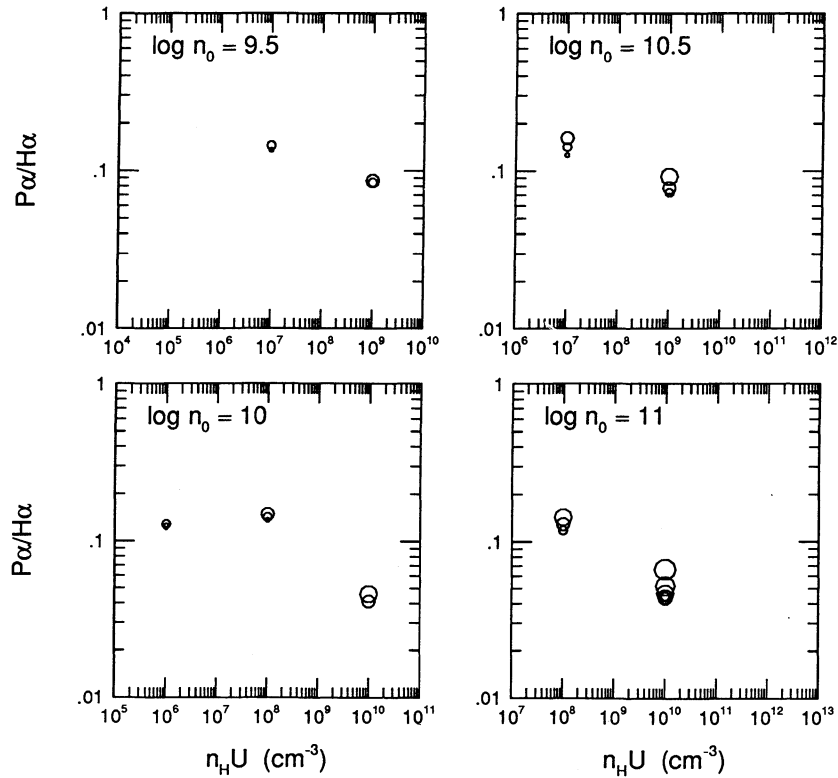
FIG. 6b

FIG. 6.—(a–c) Paα/Hα ratio from a grid of Cloudy models. The ratio is plotted against the density times the ionization parameter, so is proportional to the incident ionizing continuum flux. The larger markers represent larger column densities. For each value of the density law parameter γ (defined by $n_H \propto r^\gamma$, with Fig. 6a: $\gamma = 0$; Fig. 6b: $\gamma = -1$; Fig. 6c: $\gamma = -2$), several sequences of models that have different values of the fiducial density n_0 are individually plotted.

414
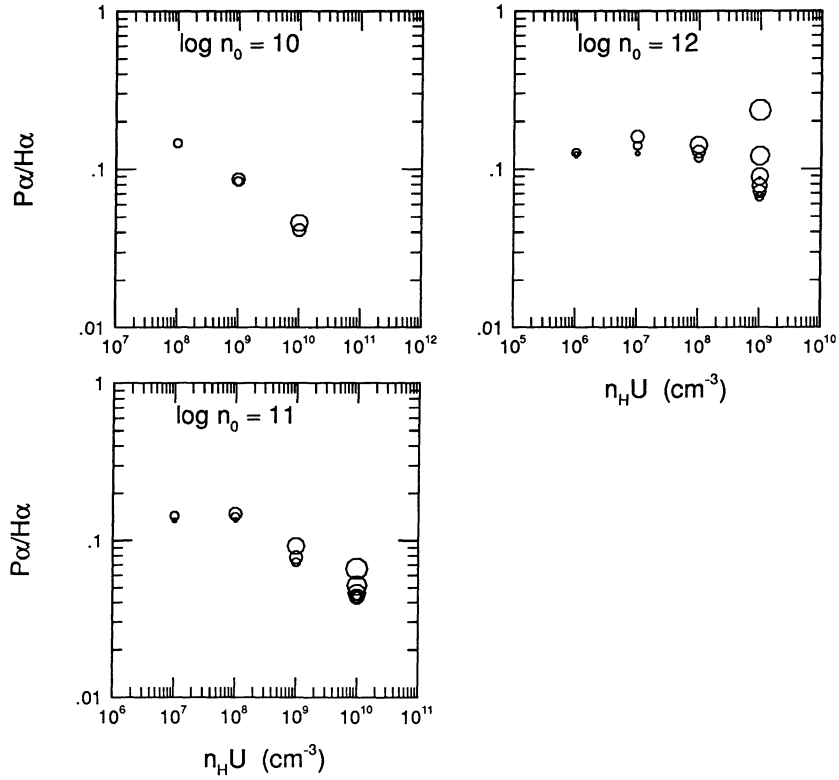
FIG. 6c
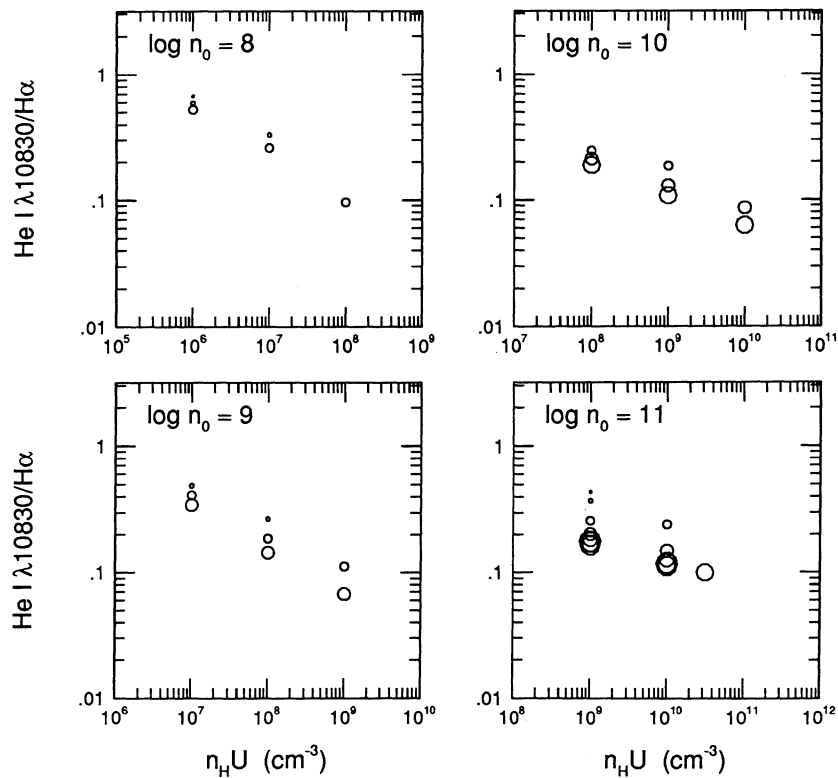
FIG. 7a

FIG. 7.—(a–c) Same as Fig. 6a–6c, for the He I λ10830/Hα ratio

415
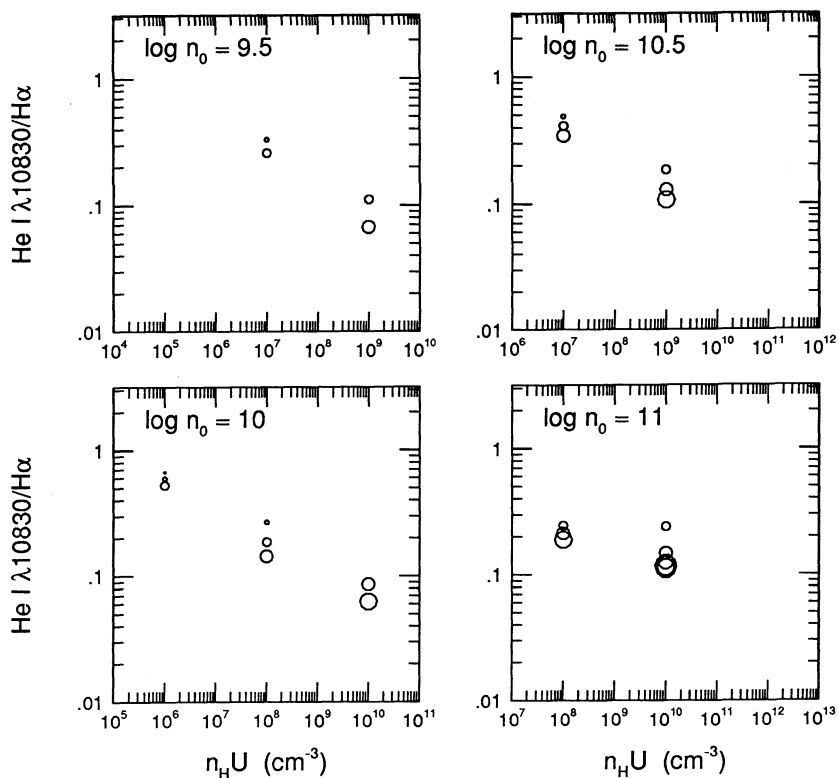
FIG. 7b
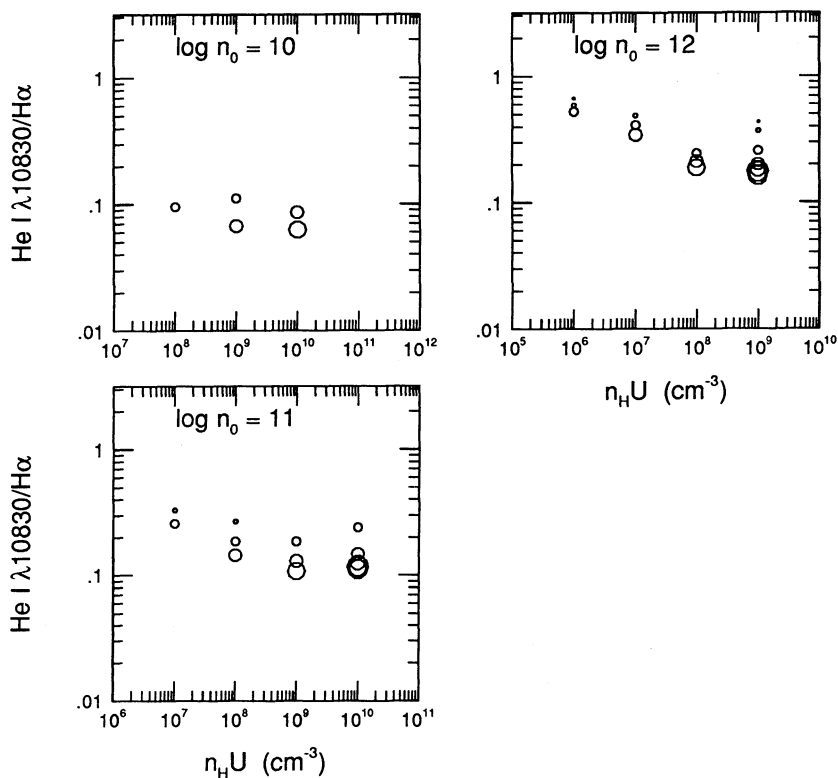
FIG. 7c

5. SUMMARY

We have presented photometric spectra of Paα and optical lines for six low-redshift QSOs, and of the He I λ10830, Paγ blend for one. We have found that most of the objects cluster in a small region of the Paα/Hα versus Hα/Hβ plot, which suggests that the Paα/Hα integrated flux ratio tends to be consistent from object to object, at least for this small sample. The one exception has a larger ratio of Paα/Hα and Hα/Hβ consistent with reddening affecting otherwise similar intrinsic ratios. Previous studies of these line ratios may have been dominated by observational uncertainties.

We also present the Paα/Hα profile ratios, at least two of which decrease with observed velocity. The decrease suggests that the higher velocity clouds experience higher incident flux by comparison with photoionization models, such as is expected of broad-line region dynamics dominated by gravity with a central continuum source. The decrease, however, raises questions as to whether the integrated Paα/Hα ratio has a consistent intrinsic value which can be used to measure reddening.

We similarly present a He I λ10830, Paγ spectrum of 1226 + 023, which we show has some suggestion that the He I/Hα ratio decreases with observed velocity. The result is inconclusive primarily because the continuum cannot be unambiguously determined, and further spectrophotometry of that part of the spectrum is required to confirm the result. The results of photoionization modeling strongly suggest that the ratio should decrease with incident flux similar to the Paα/Hα ratio.

REFERENCES

Blanco, P. R., Ward, M. J., & Wright, G. S. 1990, MNRAS, 242, 4P
Burstein, D., & Heiles, C. 1982, AJ, 87, 1165
Cochran, A. L. 1981, ApJS, 45, 73
Courvoisier, T. J.-L., Robson, E. I. Blecha, A., Bouchet, P., Hughes, D. W., Krisciunas, K., & Schwarz, H. E. 1988, Nature, 335, 330
Crenshaw, D. M. 1986, ApJS, 62, 821
Espey, B. R., Carswell, R. F., Bailey, J. A., Smith, M. G., & Ward, M. J. 1989, ApJ, 342, 666
Evans, II, N. J., & Natta, A. 1989, ApJ, 339, 943
Ferland, G. J. 1990, OSU Internal Report 90-001
Goodrich, R. W. 1990, ApJ, 355, 88
Grasdalen, G. L. 1976, ApJ, 208, L11
Hines, D. C. 1991, ApJ, 374, L9
Horne, K. 1986, PASP, 88, 609
Kühr, H., McAlary, C. W., Rudy, R. J., Strittmatter, P. A., & Rieke, G. H. 1984, ApJ, 284, L5
Kwan, J. 1984, ApJ, 283, 70
Kwan, J., & Krolik, J. H. 1981, ApJ, 250, 478
Lacy, J. H., et al. 1982, ApJ, 256, 75
Lester, D. F., Harvey, P. M., & Carr, J. S. 1988, ApJ, 329, 641
LeVan, P. D., Puetter, R. C., Smith, H. E., & Rudy, R. J. 1984, ApJ, 284, 23
McAlary, C. W., Rieke, G. H., Lebofsky, M. J., & Stocke, J. T. 1986, ApJ, 301, 105
Oke, J. B. 1964, ApJ, 140, 689
Puetter, R. C., Smith, H. E., Soifer, B. T., Willner, S. P., & Pipher, J. L. 1978, ApJ, 226, L53

Puetter, R. C., Smith, H. E., & Willner, S. P. 1979, ApJ, 227, L5
Puetter, R. C., Smith, H. E., Willner, S. P., & Pipher, J. L. 1981, ApJ, 243, 345
Rees, M. J., Netzer, H., & Ferland, G. J. 1989, ApJ, 347, 640
Rix, H-W., Carleton, N. P., Rieke, G., & Rieke, M. 1990, ApJ, 363, 480
Rudy, R. J., & Willner, S. P. 1983, ApJ, 267, L69
Savage, B. D., & Mathis, J. S. 1979, ARA&A, 17, 73
Sellgren, K., Soifer, B. T., Neugebauer, G., & Matthews, K. 1983, PASP, 95, 289
Shuder, J. M. 1982, ApJ, 259, 48
———. 1984, ApJ, 280, 491
Soifer, B. T., Neugebauer, G., Oke, J. B., & Matthews, K. 1981, ApJ, 243, 369
Soifer, B. T., Oke, J. B., Matthews, K., & Neugebauer, G. 1979, ApJ, 227, L1
Thompson, K. L. 1991, ApJ, 374, 496 (T91)
———. 1992, in preparation
Tokunaga, A. 1986, The NASA Infrared Telescope Facility Photometry Manual
Véron-Cetty, M.-P., & Véron, P. 1989, ESO Scientific Report, No. 7
Ward, M. J. 1990, Proceedings of XI European Regional Astronomy Meeting of the IAU, New Windows to the Universe, ed. Sanchez and Vazquez, Vol. II (New York: Cambridge Univ. Press), 193
Ward, M. J., Geballe, T., Smith, M., Wade, R., & Williams, P. 1987, ApJ, 316, 138
Wills, B. J., Wills, D., Evans, III, N. J., Natta, A., Thompson, K. L., Breger, M., & Sitko, M. L. 1988, ApJ, submitted
Yates, M. G., & Garden, R. P. 1989, MNRAS, 241, 167